

Benchmark of an electromagnetic gyrokinetic simulation code

K. Miki¹⁾, N. Miyato¹⁾, B. Scott²⁾, and M. Yagi¹⁾

1) National Institute for Quantum and Radiological Science: Rokkasho, Aomori 039-3212, Japan.

2) Max-Planck-Institut für Plasmaphysik, 95748 Garching, Germany.

e-mail address: miki.kazuhiro@qst.go.jp

Abstract - We introduce a benchmark of an electromagnetic gyrokinetic model, **dFEFI**. **dFEFI** solves the gyrokinetic equation, closing the system with the Poisson and induction equations. We here present a comparison of linear properties with those done by **GS2**. We examine the nonlinear turbulence with different box-sizes of L_y/L_x . For the lower L_y/L_x cases, the turbulence exhibits so bursty that higher standard deviation is estimated. The probability distribution function (PDF) analysis indicates that the bursty behavior can be related to the electron heat transport.

I. INTRODUCTION

Achievement of magnetized fusion plasma reactors requires a good confinement. However, observed anomalous transport prevents from the successful fusion reaction. Anomalous transport is believed to originate from some excitation of micro- or macro-instabilities. To solve these issues, numerical simulation of the plasma turbulent transport is now put on a main program on the achievement of ITER and DEMO scenario.

Some of recent focus on the anomalous transport put on the shortfall problem [1,2,3], i.e. the mismatch of ion/electron heat diffusivity of various simulations, in comparison with experiments; even those obtained from the various simulation codes do not match with each other.

We here present a benchmark of the electromagnetic gyrokinetic simulation code, involving electron and ion species, **dFEFI** [4]. **dFEFI** is the delta-f version of a gyrokinetic model advancing a distribution function f for both electrons and ions. **dFEFI** applies Hamada coordinate with a shifted metric, and fixed boundary condition on the radial coordinates, apart from other flux-tube local simulation codes. There is a claim that the turbulence simulation on the periodic boundary arises a mode with radially zero-wavenumber. The mode is really a fake in physics [5]. Therefore, validation of the nonlinear turbulence with the fixed boundary can be alternative to deal with the shortfall problem. Furthermore, existing simulations omit perpendicular simulation boxes in order to save the computational resources. However, due the constraint of the periodicity on the toroidal direction, the omission causes incorrect wave coupling and thus leads to premature of the estimation of turbulence transport. Therefore, correct simulation box is necessary for the accurate comparison. In addition, the radial propagation of the geodesic acoustic mode (GAM) [6], driven by the Reynolds stress of the turbulence, enhancing the turbulence spreading [7,8], can introduces a non-local effects on the turbulence transport. Once GAM is excited and starts to

propagate toward the boundary, periodic boundary will make propagation coming back from the opposite side, while the fixed boundary can shrink the propagation (or may reflect on the boundary). The behavior of the propagation will differ between the two kinds of boundaries. Thus, the fixed boundary local simulations have a potential to better assessment, since we correctly treat GAM nonlocal dynamics.

So far we have successfully reproduced the cyclone-base parameter benchmark, in comparison with other numerical simulations, **GS2** [9]. We will focus on the basic results on the **dFEFI** calculation compared with other simulation codes.

The reminder of this paper is organized as follows. In Sec. II, we introduce the model of **dFEFI** and the main features briefly. In Sec III, we examine the cyclone-base parameter on **dFEFI**. Here, we introduce linear and nonlinear dynamics of ITG turbulence. In Sec IV, we introduce a test on the box-size problem, i.e. the aspect ratio of the radial direction to the nominal. In Sec. V, we summarize this paper and remark on the local simulations.

II. DESCRIPTION OF DFEFI

dFEFI calculates a basic set of the delta-f gyrokinetic equation together with the Poisson and induction equations, as follows:

$$\frac{\partial g}{\partial t} + \frac{c}{B_0} [(J_0 \psi_e), h + f_0]_{,xy} - \frac{mz^2 + wB}{2e} K(h) + \frac{B^s}{mB} [H_0, h] = 0 \quad (1)$$

$$\sum_{sp} \int dW \left[eJ_0 g + e^2 \frac{F^M}{T} (J_0^2 - 1) \phi \right] = 0 \quad (2)$$

$$\nabla_{\perp}^2 A_{\parallel} + \sum_{sp} \frac{4\pi}{c} \int dW \left[ezJ_0 g - \frac{e^2}{c} z^2 \frac{F^M}{T} J_0^2 A_{\parallel} \right] = 0 \quad (3)$$

where the inductive response, non-adiabatic response, and gyrokinetic potential are, respectively,

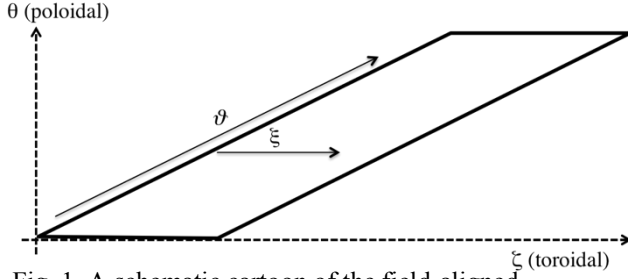


Fig. 1, A schematic cartoon of the field-aligned coordinates. The magnetic flux coordinates (θ, ζ) is replaced with the field-aligned (ϑ, ξ) .

$$g = \delta f + \frac{F^M}{T} e \frac{z}{c} J_0 A_{\parallel}, h = \delta f + \frac{F^M}{T} e J_0 \phi, \quad (4)$$

$$\psi_e = J_0 \left(\phi - \frac{z}{c} A_{\parallel} \right)$$

f_0 is the driving force given by profile gradients. Here, the gradients are fixed in time.

$$f_0 = F^M \left[\frac{1}{L_n} + \left(\frac{mv_{\parallel}^2}{T_i} - \frac{3}{2} \right) \frac{1}{L_T} \right] (-x) \quad (5)$$

The profile is fixed as a parameter L_{Ti} , L_{Te} , L_n , and F^M .

The Poisson Bracket is defined as

$$[f, g]_{ab} = \frac{\partial f}{\partial x^a} \frac{\partial g}{\partial x^b} - \frac{\partial f}{\partial x^b} \frac{\partial g}{\partial x^a}, \quad (6)$$

with a and b denoting two of the phase coordinates. The zero-th order Hamiltonian and the Maxwellian are given by

$$H_0 = m \frac{z^2}{2} + wB, \quad (7)$$

$$F^M = n(2\pi T / m)^{-3/2} \exp(-H_0 / T)$$

Here, m , e , n , T are the species background parameters of mass, charges, density and temperatures, respectively. z is parallel velocity and w is magnetic moment.

dFEFI applies Hamada coordinates with field-aligned[5]. Suppose the coordinate (V, θ, ζ) , where V is the volume labeling of the radial direction, θ is the poloidal direction, and ζ is the toroidal direction. The Jacobian is unity, i.e.

$$g^{-1/2} = \nabla V \times \nabla \theta \cdot \nabla \zeta = 1 \quad (8)$$

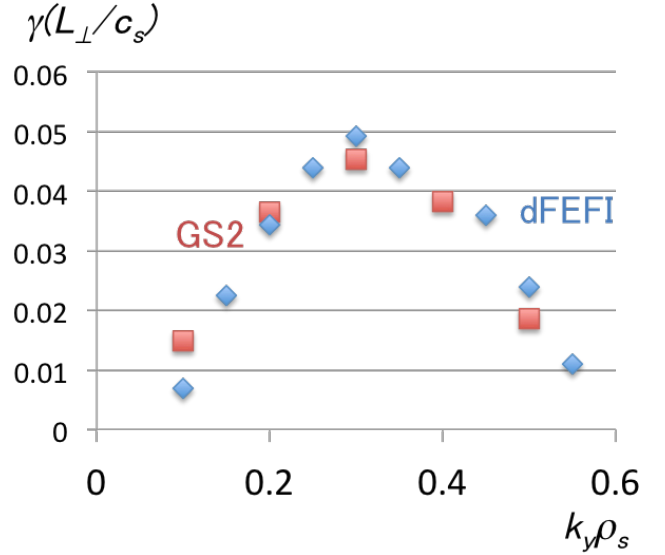


Fig.2 Plotting of the growth rate of modes for various mode wave number $k_y \rho_s$ in diamond marks. For comparison, results in GS2 are also plotted in rectangular marks.

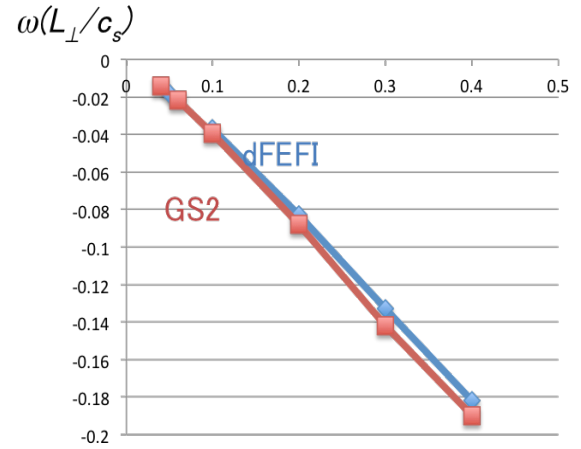


Fig.3 Plotting of the frequencies of modes for various mode wave number $k_y \rho_s$ in diamond marks. For comparison, results in GS2 are also plotted in rectangular marks.

The toroidal and poloidal periodic boundary condition can be given by

$$f(V, \theta + 2\pi, \zeta) = f(V, \theta, \zeta), f(V, \theta, \zeta + 2\pi) = f(V, \theta, \zeta). \quad (9)$$

Here we replace the coordinate into field-aligned coordinates (V, ϑ, ξ) , where ξ is the magnetic field direction and x is the nominal direction. The periodic condition can be written as

$$f(V, \vartheta + 2\pi, \xi - 2\pi q) = f(V, \vartheta, \xi),$$

$$f(V, \vartheta, \xi + 2\pi) = f(V, \vartheta, \xi). \quad (8)$$

Next, we rescale the coordinates, (x, y, s) defined by $x = (V - V_0)/V'$, $y = -\xi V'/L_{\parallel}$, and $s = L_{\parallel}$. Here x is the radial labeling with regard to volumes, y is the perpendicular direction and s is the toroidal direction. In a local computation, the necessary geometrical information is reduced to the following quantities:

$$g^{ij}(s) = \nabla i \cdot \nabla j \text{ for } \{i, j\} = \{x, y\},$$

$$b^s(s) = \frac{B_0}{B}, \quad (6)$$

$$K^{\{x,y\}}(s) = \frac{B_0 L_{\perp}}{B^2} \mathbf{B} \cdot \nabla \log B^2 \times \nabla \{x, y\}$$

where g^{ij} is for the metric, b^s is for the magnetic field, and $K^{\{x,y\}}$ is for the curvature operator. Here L_{\perp} is the local perpendicular profile scale used to normalize the dynamical equations of the model.

We apply an arbitrary shift α_k depending only on x , to

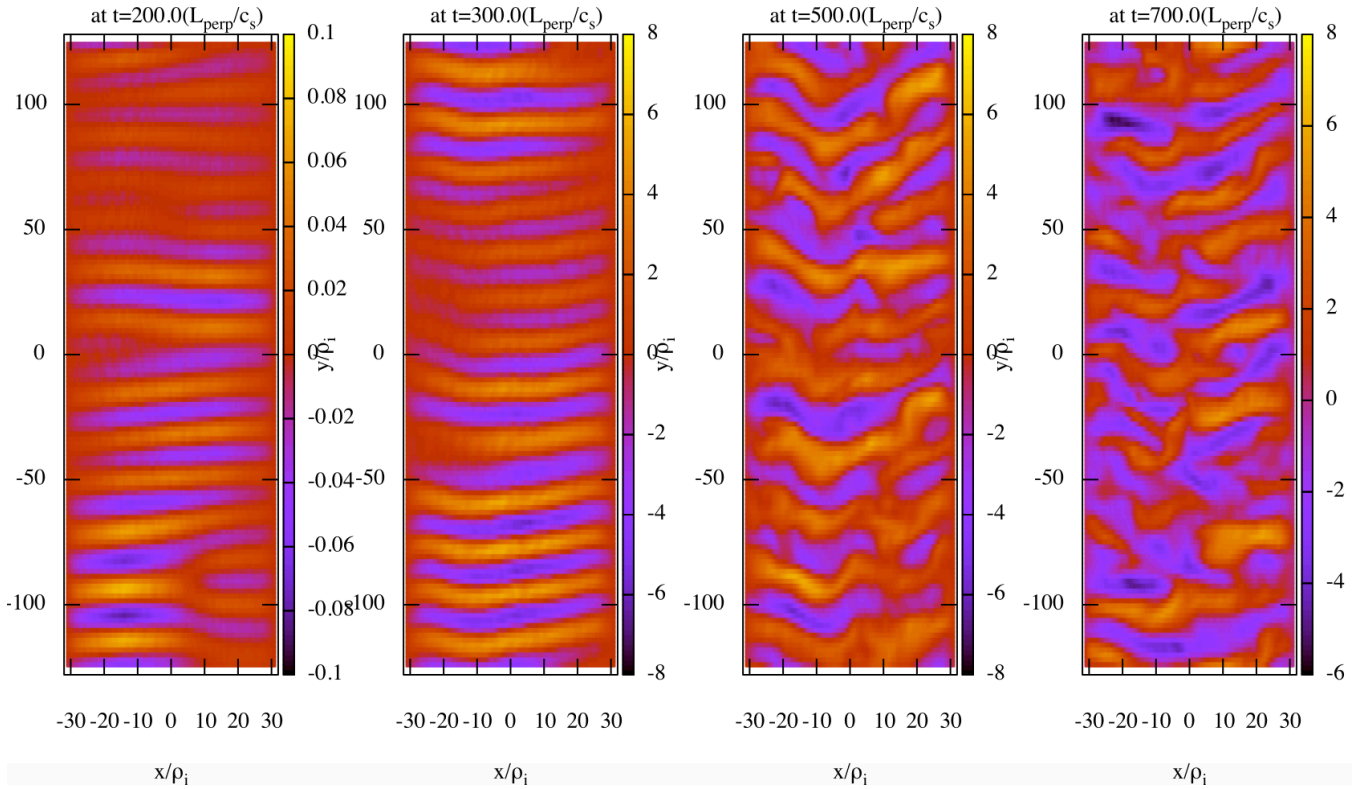


Fig.4: Contour pictures of $|e\phi/T_{\perp}|^2$ on space of (x, y) . Up to $t=300$, modes are linear, while at $t=400$, nonlinear evolution of modes appear.

the y coordinate,

$$y_k = y - \alpha_k(x),$$

$$g_{xy}^k = g_{xy} - \alpha'_k g_{xx}. \quad (7)$$

We still keep field-aligned coordinates,

$$\mathbf{B} \cdot \nabla y_k = \mathbf{B} \cdot \nabla y - \alpha'_k \mathbf{B} \cdot \nabla x = 0 \quad (8)$$

Thus, $g_k^{xy} = 0$ is identically satisfied.

III. BENCHMARK OF ITG TURBULENCE WITH CYCLONE BASE PARAMETER

We here introduce the simulation results on the ion-temperature-gradient (ITG) driven turbulence with cyclone-base parameters [9]. Poloidal section is assumed to be circular. The macro parameters are $a/R=0.184$, $L_{\perp}/R_i=0.145$, $Te/Ti=1.0$, $q=1.4$, $\hat{s}(=rq'/q)=0.78$.

$\hat{\beta}(=4\pi p_e/B^2)(qR/L_{\perp}^2)=10^{-3}$, $r_0=0.5a_0$; the system is essentially electromagnetic, but very low beta. Grid numbers are $(N_x, N_y, N_s, N_z, N_w)=(128, 128, 32, 32, 16)$.

For box size, we set $L_y/L_x=4.0$, which is relevant to the core plasma physics. We estimate L_x is comparable to the

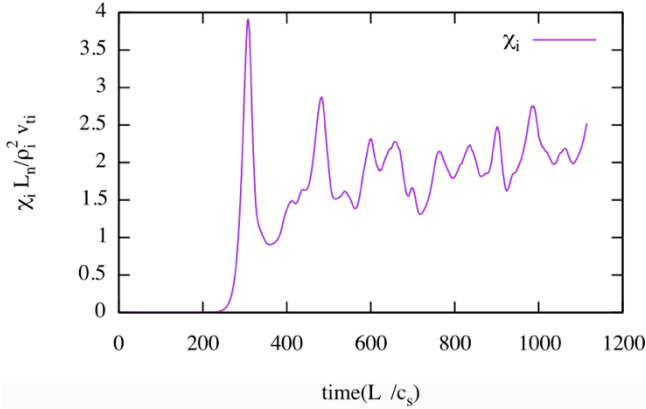


Fig. 5: Time evolution of χ_i , for the case of cyclone-base parameter.

typical perpendicular characteristic length, L_\perp . That is also comparable to the characteristic length of the density gradient, $L_\perp \sim L_n = (d \ln n / dr)^{-1}$. For the box size in y -direction, physically relevant parameter would be $L_y \sim 2\pi r_0 / q \sim 4L_x$.

In simulation, we take minimum $k_y \rho_s = 0.025$, which determines y -domain size in ρ_s unit. Here, $L_y = 2\pi / 0.025 \sim 251\rho_s$, and thus $L_x = L_y / 4 \sim 63\rho_s$. Profile gradients are given by $R/L_n = 2.2$, $R/L_{Ti} = 6.9$, and $R/L_{Te} = 6.9$. We used Helios supercomputer with 32 nodes, taking 30,000 steps ($t \sim 60(c_s/L)$) for $\Delta t = 0.002$ for 24 hours machine time. Parallelization is applied on x , s , and z discretization.

Fig. 2 shows plots of the linear growth rates of the each modes, as a function of $k_y \rho_s$. As a comparison, we also plot the linear growth rate obtained from a flux-tube code (GS2) with radial periodic boundary condition. Qualitatively dFEFI reproduces a similar peak of modes with $k_y \rho_s = 0.3$, to that of GS2. Quantitatively, in higher wave number modes ($k_y \rho_s > 0.3$), the growth rate of GS2

exhibits higher, while in the lower wave number modes ($k_y \rho_s < 0.3$), dFEFI exhibits higher growth rates.

Fig. 3 shows plots of the real frequencies of modes, as a function of $k_y \rho_s$. The real frequencies estimated by dFEFI matches with those estimated by GS2. The frequency goes negative, i.e. corresponding to the accordance with ion diamagnetic frequency. This indicates that the growing mode is related to ion-temperature-gradient (ITG) mode.

Fig. 4 shows a contour of the electric potential $|e\phi/T_i|^2$ for the case of linear ($t=100$) through nonlinear ($t=400$) phases, with each interval of 100 (L/c_s). Up to $t \sim 300$, systems are linear; radially coherent modes grow.

Fig. 5 shows a time evolution of the ion heat diffusivity χ_i in the nonlinear saturation phase. Turbulence saturates after $t=300$ (c_s/L). Averaged turbulence level is $\chi_i \sim 1.7(L_n/\rho_i c_s)$. The result is consistent with the benchmark of other gyrokinetic simulations [10].

Figs. 6 show plots of the power spectra of the potential and density fluctuations at linear and nonlinear phase. At $t=300$ (c_s/L), in the linear phase, peak is observed at $k_y \rho_i = 0.3$ where is also the peak of linear growth rate in Fig. 2. At $t=400$ (c_s/L), in the nonlinear phase, the peak of the mode shifts lower wave number, indicating the inverse cascade, which is generally seen in the fluid dynamics.

IV. DYNAMICS OF THE BOX-SIZE PROBLEM

In this section, we investigate the dynamics of turbulence. We here take physically irrelevant parameters for the cyclone-base parameter. Particularly, box-size dependency, L_y/L_x will relate to

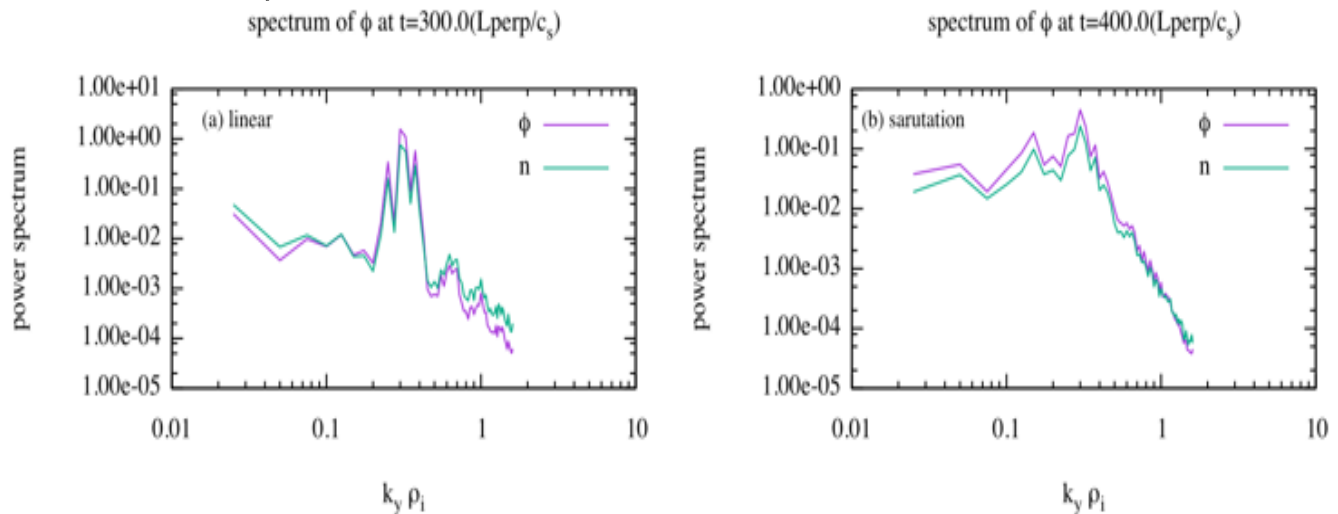


Fig.6 Plots of the power spectra of potential and density fluctuations at (a) linear $t=300$ (c_s/L), and nonlinear $t=400$ (c_s/L). A peak is observed at $k_y \rho_i = 0.3$ for the linear phase while in the nonlinear phase the peak shifts lower.

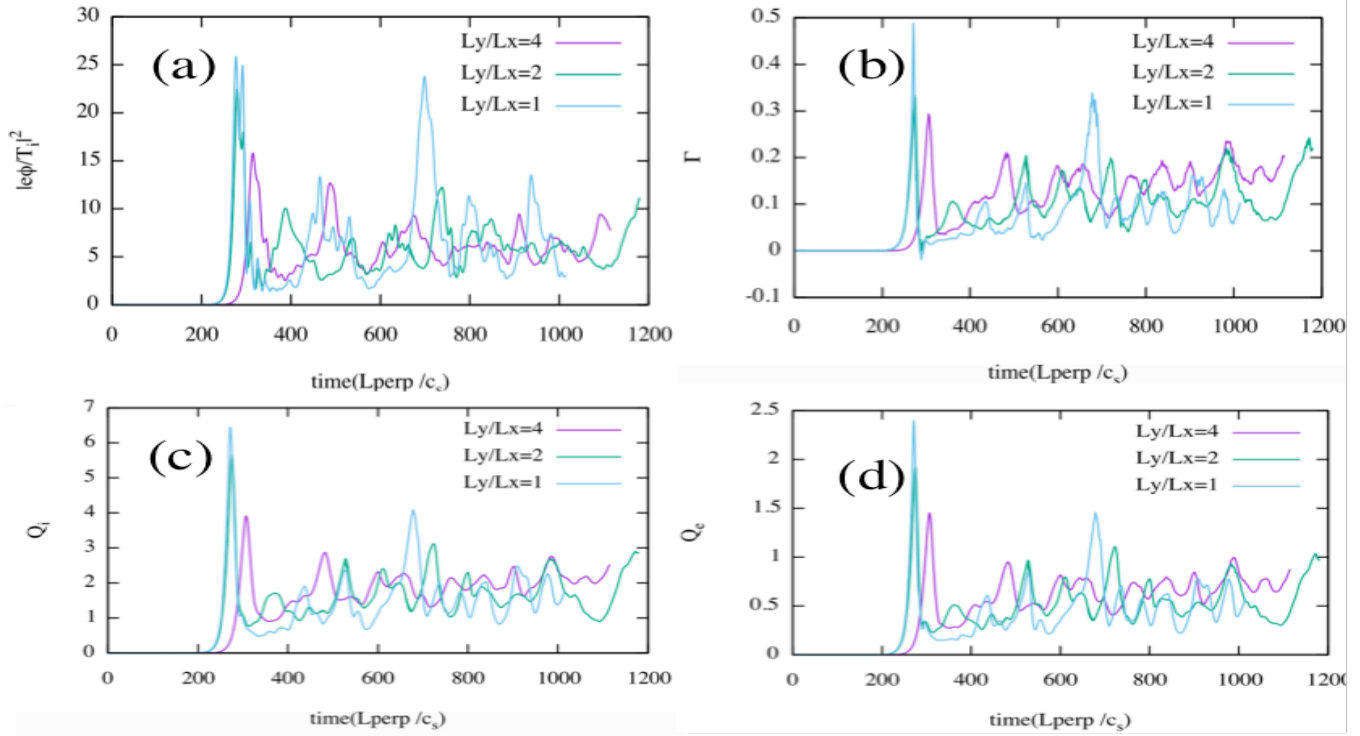


Fig. 7: Temporal evolutions of (a) $|e\phi/T_i|^2$, (b) particle flux Γ , (c) ion heat flux Q_i , and (d) electron heat flux Q_e .

the physics of the periodicity of toroidal and poloidal direction. As is discussed in Ref. [11], for the box size of x-direction $L_x \sim L_z$, the box size of y-direction in physics must be $L_y \sim 2\pi R/q$. For the cyclone-base parameter above, we estimate $L_y \sim 4L_x$. However, some existing benchmarks undergo with $L_y \sim L_x$ for the purpose of shortcut of computational time.

Once we take the shortcut of periodicity, such as $L_y \sim L_x$, this cause to take each 4 toroidal mode number $n=0, 4, 8, \dots$. They have expected that the different

results may cause in the electromagnetic physics related to the parallel dynamics, such as kinetic Alfvén waves.

Fig. 7 is the comparison of the temporal evolution of the fluctuations of turbulence for different box-sizes. We set the same parameters, but for L_y/L_x . We estimate the average level of the turbulence in the nonlinear phase (sampling $t=400-1000$). As listed in Table 1, results are $\overline{|e\tilde{\phi}/T_i|^2} = 6.17 \pm 1.18, 5.96 \pm 1.81,$

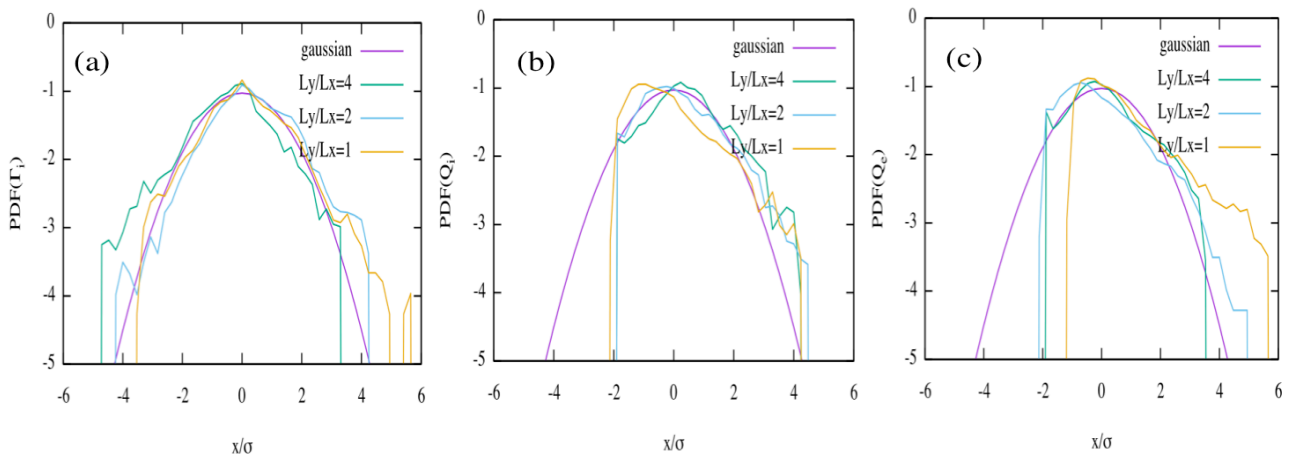


Fig. 8: Plots of probability distribution function of (a) particle flux, (b) ion heat flux, and (c) electron heat flux, with regard to x-direction. Samples are taken in the nonlinear phase, $t=400-1000$ (c_s/L_z).

| | $ e\phi/T_i ^2$ | | Q_i | | Q_e | | Γ | |
|-------------|-----------------|------|-------|-------|-------|-------|----------|--------|
| | mean | s.d. | mean | s.d. | mean | s.d. | mean | s.d. |
| $L_y/L_x=4$ | 6.17 | 1.18 | 1.74 | 0.471 | 0.579 | 0.175 | 0.119 | 0.0422 |
| $L_y/L_x=2$ | 5.96 | 1.81 | 1.77 | 0.551 | 0.599 | 0.201 | 0.118 | 0.0464 |
| $L_y/L_x=1$ | 7.00 | 4.69 | 1.67 | 0.665 | 0.53 | 0.243 | 0.101 | 0.059 |

Table 1: tables of the saturation level of ϕ^2 , Q_i , Q_e , and Γ with a normalized unit in case of $L_y/L_x=4, 2, 1$. We also list the standard deviation (s.d.).

and 7.00 ± 4.69 , for $L_y/L_x=4, 2$, and 1 , respectively, as listed in Table 1. For ion heat flux, Q_i is 1.74 ± 0.471 , 1.77 ± 0.551 , and 1.67 ± 0.665 for $L_y/L_x=4, 2$, and 1 , respectively. For electron heat flux, Q_e is 0.579 ± 0.175 , 0.599 ± 0.201 , and 0.530 ± 0.243 for $L_y/L_x=4, 2$, and 1 , respectively. Γ is 0.119 ± 0.0442 , 0.118 ± 0.0464 , and 0.101 ± 0.059 for $L_y/L_x=4, 2$, and 1 , respectively. We here notice that for every cases of the nonlinear quantities, the standard deviation (s.d.) increases as the aspect ratio L_y/L_x decreases.

The results indicate that as we shrink L_y/L_x , average turbulence level does not change. At least the difference is within the deviation. However the the standard deviation increases in higher L_y/L_x . In other words, if we cut computational cost to reduce the box size, the dynamics behaves differently in bursts. Furthermore we examine the probability distribution function (PDF) of the electron/ion heat fluxes and ion particle fluxes, shown in Fig. 8. Seen in Fig. 8 (b), PDF of ion heat flux $Q_i(x)$ tends to be along with Gaussian, but not for $x/\sigma < -3$. Instead we find some bumps on $x/\sigma \sim 4$. Nevertheless, the tendency for various box-sizes is mostly constant. For electron heat flux $Q_e(x)$, in Fig. 8(c), PDF on $L_y/L_x=1$ shows very high probability of strong heat flux exhibiting intermittency or bursts, on the other hand, the case for $L_y/L_x=4$ has not significant difference from the Gaussian curve. We also see that the PDF of particle flux for $L_y/L_x=4$ differs from that for $L_y/L_x=1$. We speculate that the difference originate from the electron dynamics, instead ions.

V. CONCLUDING REMARKS

We have presented the basic set of benchmark of the ITG turbulence with DIII-D cyclone-base parameters. dFEFI is the delta-f version of a gyrokinetic model solving both electrons and ions distribution functions. dFEFI applies Hamada coordinate, field-aligned coordinates and shifted metric. Particularly, dFEFI applies the fixed boundary condition in radial direction. This will

eliminate streamer-like modes, which are physically incorrect. Also we can treat a correct GAM dynamics without circulation of the mode propagation.

Comparison goes with the periodic flux-tube code GS2.

Using the cyclone-base parameter, we examined the main properties of ITG turbulence in the core plasmas with a circular poloidal section. We observed the growth rates of modes with a peak at $k_y r_i = 0.3$ and the mode frequency in the ion diamagnetic direction. dFEFI exhibits consistent growth rates of ITG turbulence.

We also examined the dependency of L_y/L_x , i.e. validity of eliminating modes in the ITG turbulence. Results indicate that not significant difference in the average level, while the standard deviation increases as L_y/L_x decreases.

We estimate the PDFs of turbulent fluctuation of ion and electron heat fluxes and particle flux. The electron heat flux behaves more bursty in the case of $L_y/L_x=1$ than that in the case of $L_y/L_x=4$. That can be a proof that the deviation of the bursty behavior of the case $L_y/L_x=1$.

We will be focusing on application of this work for the validation of the poloidal section in experimental tokamaks. This simulation work will shed lights on the effects of nonlocal effects of GAM to the turbulence, especially significant in the edge plasmas. Also the treatment of the fixed boundary enables us to treatment of the finite radial electric field profiles as background. The electromagnetic code with fixed boundary can also extend to the studies of turbulence in pedestal region with high β . We will focus on these issues in future work.

NOMENCLATURE

- a = minor radius
- A_{\parallel} = parallel component of the magnetic vector potential
- α_k = quantity of the shifted metric
- B = magnetic field
- B_0 = magnetic field along with toroidal direction

b_s = unit length of magnetic field along with magnetic field line
 $\hat{\beta}$ = normalized beta
 c = light speed
 c_s = sound velocity
 χ_i = ion heat diffusivity
 e = electron charge
 ϕ = electrostatic potential
 f_i = ion distribution function
 f_e = electron distribution function
 f_0 = driving force given by the gradients
 F^M = Maxwellian distribution function
 g = inductive response
 Γ = particle flux
 H_0 = zero-th order Hamiltonian
 h = non-adiabatic response
 g^{ij} = geometric factor
 J_0 = zero-th order Bessel function
 k_y = wave number in y-direction
 $K^{\{x,y\}}$ = curvature operator
 L_x = box-size of the simulation in x-direction
 L_y = box-size of the simulation in y-direction
 $L_{||}$ = characteristic length in parallel direction ($= 2\pi qR$).
 L_{\perp} = characteristic length of the profile variation
 m = mass
 n = background density
 N_x, N_y, N_s, N_z, N_w = grid numbers of (x,y,s,z,w) direction
 p_e = electron pressure
 ψ_e = gyrokinetic potential
 q = safety factor
 Q_e = electron heat flux
 Q_i = ion heat flux
 ρ_s = ion Lamor radius
 R = major radius
 s = parallel direction along with magnetic field line
 \hat{s} = magnetic field shear
 σ = standard deviation of the flux along with radial volume direction
 t = time unit
 T_e, T_i = electron/ion temperatures
 w = magnetic moment
 x = radial direction, in Hamada coordinates
 y = perpendicular direction in Hamada coordinates
 y_k = shifted perpendicular coordinates
 z = parallel velocity

REFERENCES

1. T. Görler et al., "A flux-matched gyrokinetic analysis of DIII-D L-mode turbulence", *Phys. Plasmas* **21**, 122307 (2014).
2. M. Nakata et al., "Local Gyrokinetic Vlasov Simulations with Realistic Tokamak MHD Equilibria", *Plasma and Fusion Research* **9**, 1403029 (2014).
3. X. Garbet and Y. Idomura et al., "Gyrokinetic simulations on turbulence transport", *Nucl. Fusion* **50**, 043002 (2010).
4. B. Scott, "Derivation via free conservation constraints of gyrofluid equations with finite-gyroradius electromagnetic nonlinearities" *Phys. Plasmas* **17**, 102306 (2010).
5. B. Scott, "Shifted metric procedure for flux tube treatments of toroidal geometry: Avoiding grid deformation", *Phys. Plasmas* **8**, 447 (2001).
6. N. Winsor et al., "Geodesic Acoustic Waves in Hydromagnetic Systems", *Phys. Rev. Lett.* **11**, 2448 (1968).
6. K. Miki et al., "Intermittent transport associated with the geodesic acoustic mode near the critical gradient regime", *Phys. Rev. Lett.* **99**, 145003 (2007).
7. K. Miki et al., "Role of the geodesic acoustic mode shearing feedback loop in transport bifurcations and turbulence spreading", *Phys. Plasmas* **17**, 032309 (2010).
8. T.S. Hahm and P.H. Diamond et al., "Turbulence spreading into the linearly stable zone and transport scaling", *Plasma Phys. Control. Fusion* **46**, A323 (2004).
9. W. Dorland et al., "Electron Temperature Gradient Turbulence", *Phys. Rev. Lett.* **85**, 5579 (2000).
10. A. M. Dimits et al., "Comparisons and physics basis of tokamak transport models and turbulence simulations", *Phys. Plasmas* **7**, 969 (2000).
11. B. Scott "Global consistency for thin flux tube treatments of toroidal geometry", *Phys. Plasmas* **5**, 2334 (1998).

ACKNOWLEDGMENTS

This work was supported by the Helios supercomputer at IFERC-CSC under the projects GKNETLH and CEPC. The author K.M. thanks Y. Kishimoto and H. Sugama for helpful discussion.